Theoret. Comput. Fluid Dynamics (2001) 14: 337–358

Theoretical and Computational Fluid Dynamics

Direct Numerical Simulation of Turbulent Flow over a Rectangular Trailing Edge*

Y.F. Yao, T.G. Thomas, and N.D. Sandham

School of Engineering Sciences, University of Southampton,
Highfield, Southampton SO17 1BJ, England

J.J.R. Williams

Department of Engineering, Queen Mary and Westfield College,
Mile End Road, London E1 4NS, England

Communicated by R.D. Moser

Received 4 March 1999 and accepted 27 October 2000

Abstract. This paper describes a direct numerical simulation (DNS) study of turbulent flow over a rectangular trailing edge at a Reynolds number of 1000, based on the freestream quantities and the trailing edge thickness h; the incoming boundary layer displacement thickness δ^* is approximately equal to h. The time-dependent inflow boundary condition is provided by a separate turbulent boundary layer simulation which is in good agreement with existing computational and experimental data. The turbulent trailing edge flow simulation is carried out using a parallel multi-block code based on finite difference methods and using a multi-grid Poisson solver. The turbulent flow in the near-wake region of the trailing edge has been studied first for the effects of domain size and grid resolution. Then two simulations with a total of $256 \times 512 \times 64$ ($\sim 8.4 \times 10^6$) and $512 \times 1024 \times 128$ ($\sim 6.7 \times 10^7$) grid points in the computational domain are carried out to investigate the key flow features. Visualization of the instantaneous flow field is used to investigate the complex fluid dynamics taking place in the near-wake region; of particular importance is the interaction between the large-scale spanwise, or Kármán, vortices and the small-scale quasi-streamwise vortices contained within the inflow boundary layer. Comparisons of turbulence statistics including the mean flow quantities are presented, as well as the pressure distributions over the trailing edge. A spectral analysis applied to the force coefficient in the wall normal direction shows that the main shedding frequency is characterized by a Strouhal number based on h of approximately 0.118. Finally, the turbulence kinetic energy budget is analysed.

1. Introduction

The problem of turbulent flow over a rectangular trailing edge geometry is closely related to that of predicting the drag force acting on an airfoil with a blunt trailing edge or the pressure loss behind a blunt gas turbine blade, and consequently it has important practical applications in the aerospace industry. This flow has proved difficult to model accurately due to the abrupt change in the flow structure that takes place at

* This work has been supported by the UK Engineering and Physical Science Research Council (EPSRC) through the financial and parallel computer grants GR/L 18570 and GR/M 08424.

the rear separation point: upstream it is a boundary layer flow, and downstream it is a wake flow. In the immediate vicinity of the trailing edge the flow can be locally far from an equilibrium state and conventional turbulence modelling techniques either prove to be inadequate or require special *ad hoc* modifications. However, this class of problem is suitable for the direct numerical simulation (DNS) technique; the method is able to achieve accurate simulations of the unsteady turbulent fluid motions including the full range of scales provided that the finite difference grid has sufficient resolution, typically slightly larger than the Kolmogorov microscale. Experience has shown that good quality results can be obtained from simulations at a moderate Reynolds number.

One of the earliest experimental studies of the trailing edge flow is due to Black (1975) who investigated a two-dimensional strut with a semi-circular leading edge and an asymmetric bevelled trailing edge of 25° tip angle. Similar experiments were carried out later by Viswanath and Brown (1983), Nakayama (1984) and Thompson and Whitelaw (1985), using different trailing edge tip angles. All these experiments considered the flow at a high angle of attack in which the separation occurred with an extended region of recirculation on the upper surface upstream of the trailing edge; attention was focused on this as well as on the near-wake region downstream. A numerical study of the same geometric configuration of Black (1975) has been carried out recently by Wang (1997) using large-eddy simulation (LES) techniques for both the flow and the aeroacoustic behaviour. Flows over an even simpler geometry such as a rectangular trailing edge with a finite thickness are also of interest. Unlike the bevelled trailing edge described above, the flow past the rectangular trailing edge is characterized by fixed separation points at the sharp corners. As a result, the wake exhibits complicated fluid dynamics even at a moderate Reynolds number, and is amenable to a DNS study using currently available computer resources.

The blunt trailing edge flow is quite similar in behaviour to the classical bluff body problem of flow past a circular cylinder, and much of the fundamental behaviour, such as the large-scale vortex shedding into the wake, is qualitatively similar. Recent reviews of the current state of the art in bluff body flows have been given by Roshko (1993) and Bearman (1998). There are, however, clear differences between the present trailing edge problem and the cylinder problem concerning the specification of the inflow: in the present trailing edge simulation the inflow contains an existing turbulent flow field which interacts with and modifies the classical unsteady wake flow.

There have been several previous experimental and numerical studies of flow over the rectangular trailing edge arrangement with two incoming boundary layers. For laminar flow at low Reynolds number, it is known that the region immediately behind the trailing edge is one of absolute instability, and downstream in the wake the flow becomes convectively unstable. Thus the flow at the trailing edge has the characteristics of an oscillator, and the flow downstream has the characteristics of an amplifier. These stability properties have been studied by Hannemann and Oertel (1989) using both numerical calculations and linear stability analysis. The experimental study of Hannemann *et al.* (1986) also considered the near-wake region of a rectangular trailing edge at low Reynolds number.

For turbulent flow with symmetric boundary layers on the upper and lower surfaces of the rectangular trailing edge, an experimental study has been carried out by Gough and Hancock (1996). The inflow boundary layer thickness (δ_{99}) at the trailing edge was equal to ten times the trailing edge thickness h, and the Reynolds number (based on the momentum thickness θ) was about 600. For this configuration it was found that the mean recirculation region extended for about $3h$ downstream of the trailing edge, and the coherent Kármán vortex street was evident up to about $10h$, beyond which it became incoherent and was effectively scrambled by the small-scale streamwise vortices. A similar flow was investigated computationally by Gao *et al.* (1996) using the LES technique. They found generally good qualitative agreements with the experimental data for various turbulence statistics but quantitative differences were clearly evident; these have been attributed to influences from the inflow boundary condition, as well as the models and numerics used in the simulation. It is believed that the upstream incoming flow has a strong influence on the downstream flow field, and hence that an accurate simulation of the inflow turbulent boundary layer is a necessary requirement for performing an accurate trailing edge flow simulation.

The overall arrangement of the present simulation is outlined in Figure 1. A turbulent flow over a rectangular trailing edge geometry at a Reynolds number of 1000, based on the freestream quantities and the trailing edge thickness h, is studied using the DNS technique. Similar to Gao *et al.* (1996), the time-dependent inflow boundary condition was generated from a separate turbulent boundary layer flow simulation (called the "precursor" simulation); this simulation is validated by comparison with existing computational and ex-

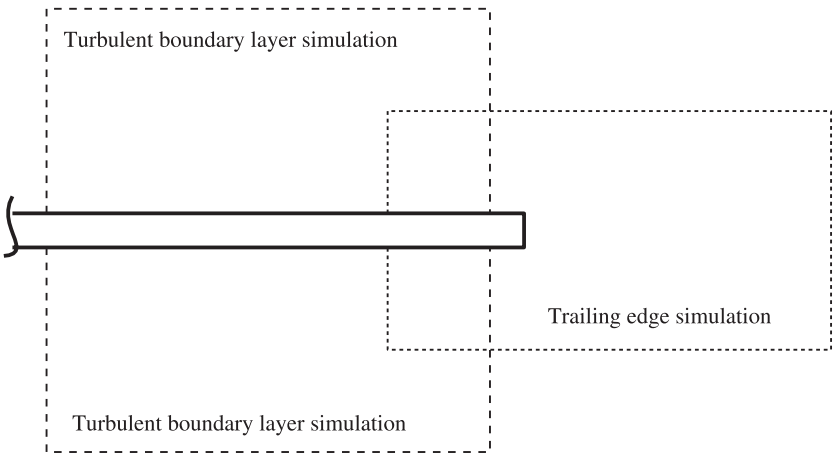

Figure 1. Configurations of turbulent boundary layer and trailing edge flow simulations.

perimental data. Then a turbulent trailing edge flow simulation (called the "successor" simulation) is carried out using a parallel multi-block DNS code based on a finite difference method with a multi-grid Poisson solver. The turbulent flow in the near-wake region of the trailing edge is tested for the influence of the computational domain size and grid resolution used. Two simulations with a total of $256 \times 512 \times 64$ ($\sim 8.4 \times 10^6$) and $512 \times 1024 \times 128$ ($\sim 6.7 \times 10^7$) grid points in the computational domain are used to investigate the flow features. Visualization of the instantaneous flow field shows clearly the interactions between the large-scale spanwise, or Kármán, vortices and the small-scale streamwise vortices which formed part of the incoming boundary layer turbulence, and provides an insight into the complex fluid dynamics in the near-wake region. Comparisons of mean flow quantities and turbulence statistics are presented, as well as the pressure distributions over the trailing edge. A spectral analysis using the time history of the force coefficient in the wall normal direction is carried out and turbulence kinetic energy budget analysis is performed at locations in both the boundary layer and wake regions.

2. Governing Equations and Numerical Discretization

We consider here the motion of an incompressible viscous fluid past a rectangular trailing edge. The fluid, assumed to have constant density ρ and constant dynamic viscosity μ (thus the kinematic viscosity $\nu = \mu/\rho$ is also a constant), moves in a Cartesian coordinate system $x_i = (x, y, z)$ with velocity $u_i = (u, v, w)$ and pressure p. Let t denote the time, then the evolution of the fluid motion satisfies the incompressible Navier–Stokes equations given by

$$\frac{\partial u_i}{\partial t} + \frac{\partial u_j u_i}{\partial x_j} = -\frac{1}{\rho}\frac{\partial p}{\partial x_i} + \frac{1}{Re}\frac{\partial^2 u_i}{\partial x_j \, \partial x_j} \tag{1}$$

and

$$\frac{\partial u_i}{\partial x_i} = 0\,, \tag{2}$$

where we use the usual tensor summation convention for indices i and j. We also define the Reynolds number $Re = U_e h/\nu$ for this problem in terms of the freestream flow velocity U_e and the trailing edge thickness h.

The Navier–Stokes equations are discretized on a staggered grid using a second-order central finite difference scheme, and advanced in time with the projection method based on a second-order explicit Adams–Bashforth scheme. The provisional velocity u_i^* is projected using the data from the current time step n and previous time step $n-1$ as

$$\frac{u_i^* - u_i^n}{\Delta t} = \frac{3}{2}H_i^n - \frac{1}{2}H_i^{n-1} + \frac{1}{2}\frac{\partial p^{n-1}}{\partial x_i}, \tag{3}$$

where the quantity H_i is defined as

$$H_i = -\frac{\partial u_j u_i}{\partial x_j} + \nu \frac{\partial^2 u_i}{\partial x_j \, \partial x_j}.$$

This is then corrected for continuity to yield the velocity at a time step $n+1$ using

$$u_i^{n+1} = u_i^* - \frac{3}{2}\Delta t \frac{\partial p^n}{\partial x_i}, \tag{4}$$

where the pressure p^n is obtained by the solution of the Poisson equation

$$\frac{\partial^2 p^n}{\partial x_i \, \partial x_i} = \frac{2}{3\Delta t} \frac{\partial u_i^*}{\partial x_i}. \tag{5}$$

The use of a fully explicit scheme in both the time and the space is efficient in terms of computer storage, but can be restricted by the viscous CFL limit if the computational grid is excessively fine near a solid boundary. We have used the grid stretching function in the wall-normal direction given by

$$y = \left[a\eta + (1-a)\left(1 - \frac{\tanh(b(1-\eta))}{\tanh(\eta)}\right)\right] y_l, \tag{6}$$

for the precursor simulation, where y is the wall distance, y_l is the domain height, η is uniformly spaced with n cells in the range [0, 1], and the coefficients a and b are used to control the stretch ratio ($a = 0.1$ and $b = 4.0$ are used in the simulation). Here the near-wall grid size is $O(1/n)$, as distinct from $O(1/n^2)$ for a cosine-type grid (see, for example, Kleiser and Schumann, 1980), and in this case the CFL limit is not unduly restrictive. In the successor simulation uniform grids are used in all three directions for reasons of computational efficiency, and the CFL restriction is essentially unchanged.

The solution methods for the Poisson equation (5) differ for the precursor and successor simulations; the precursor uses the modified Fourier-based method described in Section 3.1, and the successor simulation uses an efficient parallel multi-grid technique.

3. Boundary Layer Flow Simulation

The turbulent boundary layer (precursor) simulation is performed using the temporal DNS code of Sandham (1994) with the modifications described below to enable a spatially developing boundary layer to be computed. The spatial development breaks the streamwise periodicity assumed in the temporal plane channel simulation code and the conventional technique of recycling the turbulence many times though the computational box has to be modified to incorporate some form of scaling transformation.

One method of reformulating the spatially developing boundary layer problem so that the computational variables are effectively homogeneous in the streamwise direction is to use a similarity transformation, analogous to that used in the first-order laminar boundary layer theory, and to work in terms of the resulting similarity coordinates. This has been done previously by Spalart and Leonard (1985) and Spalart (1988). The method worked quite effectively as it permits the streamwise fast Fourier transforms (FFTs) to be retained, although with the additional penalty of several extra (and also complicated) "growth" terms added to the equations.

An alternative approach which avoids the extra terms is to use a feedback device with re-scaling (Lund *et al.*, 1996, 1998). In effect an approximate artificial inflow is constructed based on re-scaling the flow variables at a plane near the outlet. Such a re-scaling procedure is chosen to compensate for the spatial boundary layer growth between the re-scaling and the inflow planes exactly. An additional complicating feature is that the inner and outer parts of the boundary layer profile scale differently: the inner on the friction velocity, and the outer on the defect velocity. The method has been shown to yield results that compare well with those from other methods, but at a relatively lower cost (in terms of CPU and memory). Such a methodology has been used successfully to generate the instantaneous turbulent inflow data for the LES of trailing edge (Wang, 1997) and bump flows (Wu and Squires, 1998); the same method will be adopted in the precursor simulation described.

3.1. Solution of the Pressure Equation

It is clearly desirable, in terms of computational efficiency, to arrange for the solution of the Poisson equation to be done using the FFTs in the planes parallel to the wall, similar to that adopted in the homogeneous plane channel flow simulation. However, it is not immediately clear that this can be done for a spatially developing flow simulation. The computational problem for the pressure field (in the streamwise direction) resolves itself into the discretization of a $\partial^2/\partial x^2$ operator with homogeneous boundary conditions for the gradient $\partial/\partial x = 0$ at the cell face at each end of the domain. This suggests either a cosine Fourier transformation on the interval $[0, \pi]$ or a Fourier transform on the interval $[0, 2\pi]$ but with the imaginary part enforced to zero in the Fourier space (equivalent to a cosine Fourier transformation). The latter treatments are used at present in order to retain the methodology of FFTs which already existed in the code, although it is obviously more efficient to use the former. As the pressure variables are stored at the cell centre and subsequently are not coincident with the boundary conditions assumed on the cell faces, a phase shift with half a grid spacing is then required. The solution process can be described as follows. The data is extended by adding its mirror image to one end, thus constructing a periodic function in the extended box. The conventional FFTs are then applied, followed by a forward phase shift by multiplying with a factor $e^{i(k(\Delta x/2))}$, where k is the wave number and Δx is the grid spacing. In the Fourier space the imaginary part is set to zero to satisfy the boundary conditions and also to enforce a cosine Fourier transformation. The data is then backward phase shifted using a factor $e^{-i(k(\Delta x/2))}$ and an inverse transformation back to physical space is applied. The solution of pressure in the wall normal direction is carried out using a conventional tridiagonal inversion method. Finally the data of the mirror image part is removed and not used in the velocity field calculations. This solution method has been validated by inspection of residuals as an independent routine on a variety of source functions, and further in the complete code for a laminar Blasius boundary layer flow simulation.

3.2. Simulation Parameter and Inflow Condition

The turbulent boundary layer (precursor) simulation is started with a laminar transitional process with artificial excitation at the inlet and using an extended box. The simulation is advanced in time and the flow undergoes an artificial transition producing fine-scale turbulence. The additional resolution required is provided by shortening the box with a fixed number of grid points rather than extending the grid. This procedure avoids the need to re-grid but introduces transients which require additional simulation time to disappear. The whole simulation is able to run on a desktop workstation. Once the flow is fully turbulent the simulation is continued using Lund's re-scaling method. The final computation box size is $50 \times 20 \times 6$ (in units of δ^*_{in}, the boundary layer displacement thickness at the inlet) in the streamwise (x), wall-normal (y) and spanwise (z) directions, respectively, and uses a $128 \times 96 \times 64$ grid. The grid is stretched in the wall-normal direction and provides a near-wall resolution of $\Delta x^+ = 19$, $\Delta y_1^+ = 0.5$, $\Delta z^+ = 4.5$ and thus gives about 10–12 points in the viscous sublayer ($y^+ \leq 10$).

The boundary conditions are as follows: a periodic condition is applied in the spanwise direction; a no-slip condition is used on the solid wall; a slip condition with mass continuity is used on the free surface plane; a convective condition for the outflow plane; and instantaneous inflow conditions for the inflow plane.

The details of the re-scaling method can be found in Lund *et al.* (1996, 1998). Only the main procedures of generating the inflow data are highlighted here.

(1) The instantaneous velocity u_i is decomposed into a mean part U_i (i.e. averaged in time and the spanwise direction) and a fluctuation part u_i':

$$u_i(x, y, z, t) = U_i(x, y) + u_i'(x, y, z, t). \tag{7}$$

(2) The mean part is then re-scaled in both the inner and outer regions according to the wall and defect laws, respectively. Taking the scaling process in the streamwise direction as an example, we have the law of the wall in the inner region

$$U^{\text{inner}} = u_\tau(x) f_1(y^+), \tag{8}$$

and the defect law in the outer region

$$U_e - U^{\text{outer}} = u_\tau(x) f_2(\eta), \tag{9}$$

where $u_\tau(x)$ is the friction velocity, $y^+ = u_\tau y/\nu$ represents the wall units coordinate, $\eta = y/\delta_{99}$ is the defect coordinate and the functions f_1 and f_2 are assumed universal. Hence we can derive the relations between the inlet plane (denoted inlt) and one downstream plane (denoted recy) as

$$U_{\text{inlt}}^{\text{inner}} = \gamma U_{\text{recy}}\left(y_{\text{inlt}}^+\right), \tag{10}$$

$$U_{\text{inlt}}^{\text{outer}} = \gamma U_{\text{recy}}(\eta_{\text{inlt}}) + (1-\gamma)U_e, \tag{11}$$

where $\gamma = u_{\tau,\text{inlt}}/u_{\tau,\text{recy}}$, and $U_{\text{recy}}(y_{\text{inlt}}^+)$ and $U_{\text{recy}}(\eta_{\text{inlt}})$, are the mean velocities at the recycling plane but expressed on the grid coordinates (y^+ and η_{inlt}, respectively) of the inlet plane. Some interpolation is required in the wall-normal direction to match grids.

(3) The fluctuation part is also re-scaled by assuming that it can be decomposed as

$$\left(u_i'\right)^{\text{inner}} = u_\tau(x) g_i(x, y^+, z, t), \tag{12}$$

$$\left(u_i'\right)^{\text{outer}} = u_\tau(x) h_i(x, \eta, z, t). \tag{13}$$

The functions g_i and h_i are supposed to be approximately homogeneous in the streamwise direction and therefore a "periodic" condition can be used. This results in

$$\left(u_i'\right)_{\text{inlt}}^{\text{inner}} = \gamma\left(u_i'\right)_{\text{recy}}\left(y_{\text{inlt}}^+, z, t\right), \tag{14}$$

$$\left(u_i'\right)_{\text{inlt}}^{\text{outer}} = \gamma\left(u_i'\right)_{\text{recy}}(\eta_{\text{inlt}}, z, t). \tag{15}$$

(4) The whole velocity profile is finally reconstructed at the inlet plane through a weighted-averaging procedure by combining the re-scaled inner and outer parts.

(5) To achieve a targeted quantity (e.g. the momentum thickness θ) at the inflow plane as the required inflow condition, an additional procedure of correction is used at each time step by iteratively adjusting the inlet boundary layer thickness to ensure this specified profile value at the inlet plane.

3.3. Results and Discussion

The efficient pressure solver with phase shifting and the re-scaling method described above are used to perform the DNS of a spatially developing incompressible turbulent boundary layer with zero pressure gradient in the streamwise direction. Results from this simulation are consistent with earlier studies. Figure 2 gives the friction velocity (u_τ) of the present DNS result (at a position where $Re_\theta = 670$), including comparisons with results from Spalart and Leonard (1985) for $Re_\theta = 690$ and experimental data (Purtell *et al.*, 1981) for $Re_\theta = 500$–860. In general a good agreement is achieved. The shape factors also compare well, with 1.50 from the present simulation, 1.52 estimated from Spalart and Leonard and 1.49 estimated from Purtell. Figure 3 shows the streamwise mean velocity profile U^+ against the wall-normal coordinate y^+ (in wall units). Data from Spalart and Leonard's calculation are re-plotted in the same picture, which shows good agreement. Also both computations agree well with the linear and logarithmic profiles (with $\kappa = 0.39$, $b = 4.2$). Figure 4 gives the root-mean-square (rms) value of turbulence statistics U_{rms}, V_{rms} and W_{rms} (normalized by u_τ) against the defect coordinate η ($= y/\delta_{99}$). Comparisons with the data of Spalart and Leonard's simulation and the experimental data of Klebanoff (1954) are also made. An overall good agreement is again achieved. Figure 5 gives the instantaneous fluctuation velocity u' contours (at the plane of $y^+ = 10$), where the streaks are clearly shown. In conclusion it is found that the method adopted gives realistic turbulent boundary layer data to be used as the inflow conditions for the trailing edge flow simulation.

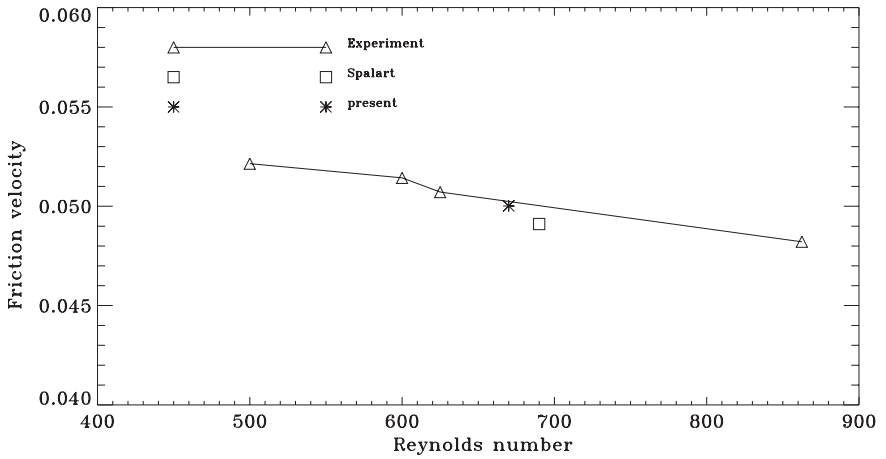

Figure 2. Comparisons of friction velocity (u_τ) in the turbulent boundary layer simulation. Star: present DNS; open square: DNS of Spalart and Leonard (1985); solid line with open triangle: experimental data from Purtell *et al.* (1981). Reynolds number is based on the momentum thickness θ.

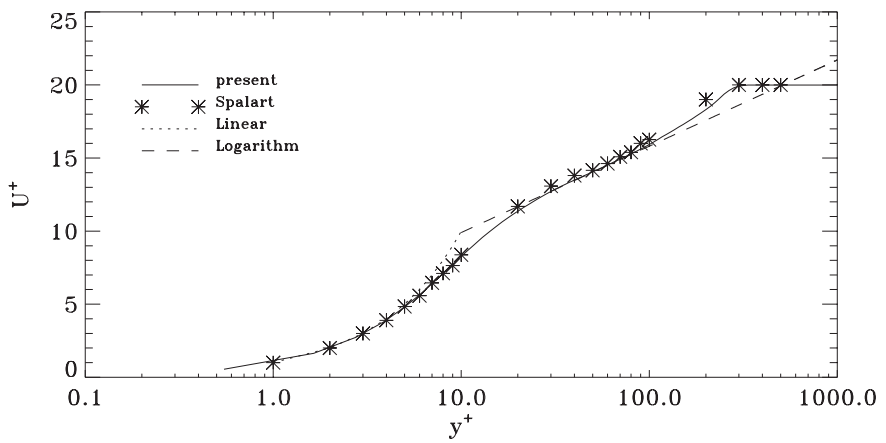

Figure 3. Mean velocity profile in the turbulent boundary layer simulation in comparison with the data of Spalart and Leonard's DNS (star) and the linear (dotted line) and logarithm (dashed line, $\kappa = 0.39$, $b = 4.2$).

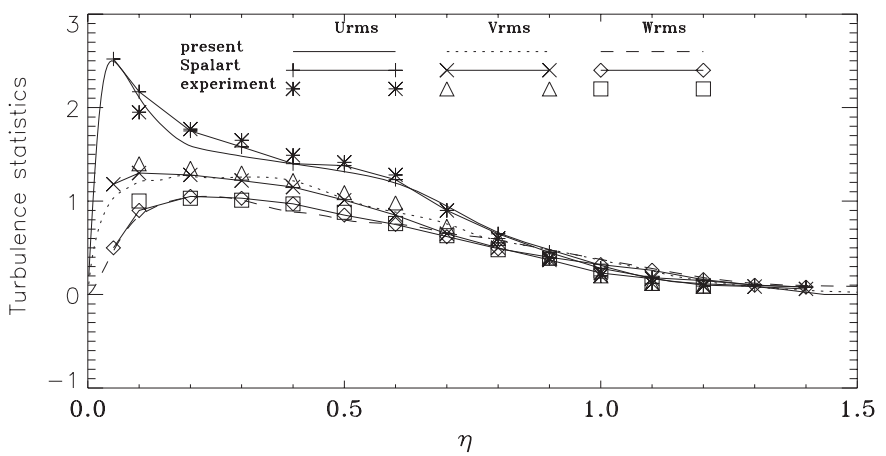

Figure 4. Turbulence statistics $U_{\rm rms}$, $V_{\rm rms}$ and $W_{\rm rms}$ profiles in the turbulent boundary layer simulation in comparison with the data of Spalart and Leonard's DNS and experimental data of Klebanoff (1954).

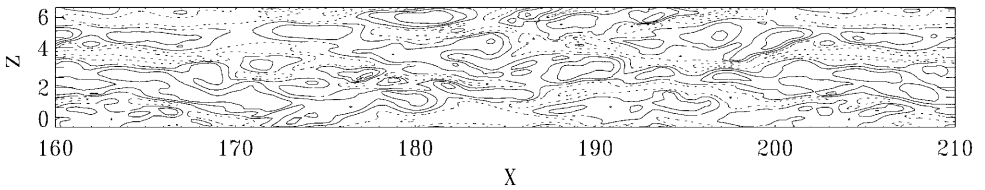

Figure 5. Instantaneous fluctuation velocity $u'(= u - \bar{u})$ contours at a plane where $y^+ = 10$. Dashed lines: low speed; solid lines: high speed.

3.4. Sampling Procedure

After the turbulent boundary layer flow has fully developed, another two runs are made for the collection of data in time sequences to be used for the upper and lower inflow boundary layers for the trailing edge problem. These two data sets should be statistically converged but un-correlated in time. The collection is taken at a plane where $\delta^* \sim 1$. The wall-normal and spanwise sizes of the collection plane have to be the same as those defined in the trailing edge flow simulation (see Figure 7(b) for reference). The coordinates of grid points in the "precursor" and "successor" simulations are generally different and a bi-linear interpolation procedure is used. The interpolation errors will be minimized, provided that both the "precursor" boundary layer simulation and "successor" trailing edge simulation have similar grid resolution especially in the near wall region. The accuracy will be affected if a lower grid resolution is used in the latter. Also the data in the boundary layer simulation has to be truncated in the wall-normal direction because the height ($20\delta^*_{\text{in}}$) is larger than that used later in the trailing edge simulation. The slice plane is divided into several panels (a total number of 60 in the present simulation, which consist of 32 on the upper side and 28 on the lower side; see Figure 7(b)), each corresponding to one face of the block at the inflow plane. A total of 4000 planes of data (equivalent to 200 time units) from the turbulent boundary layer simulation are stored in the slice files. The data can be used for fluid travelling at the freestream velocity to pass through the computational box for the trailing edge simulation ten times, which is sufficient based on previous tests.

4. Trailing Edge Flow Simulation

The term DNS implies that turbulence eddy motions with all length scales in the flow have been properly resolved. This requires the computational grid to be fine enough to represent the smallest turbulence eddy motions and consequently large computer resources are generally required. For the present trailing edge flow simulation we adopt a computational box of relatively small size, but large enough to include the trailing edge geometry and also the development of the incoming turbulent boundary layer flow.

Simulations are made for comparison of the effects of changing the computational box size and improving the grid resolution. Finally two high-resolution simulations are carried out for investigating the key flow features in detail. Visualization of instantaneous flow structures are provided for a close look at the interactions between the large-scale spanwise Kármán vortices and small-scale streamwise vortices in the wake region. Turbulence statistics are compared, as well as the pressure distributions over the trailing edge. A spectral analysis of the force coefficient in the wall-normal direction is performed, and finally the turbulence kinetic energy budget is analysed.

4.1. Problem Definition and Computational Domain

The computational box for the trailing edge flow (successor) simulation is shown in Figure 6. The coordinate origin is at the centre of the downstream face of the trailing edge. A baseline simulation (named case A) for reference is set up with a box size of $20h \times 16h \times 6h$ in the streamwise (x), wall-normal (y) and spanwise (z) directions, respectively. The length in the streamwise direction (denoted as L_X) includes $5h$ along the trailing edge plate and $15h$ in the wake region. The $5h$ distance of the plate is used for further development of the incoming turbulent boundary layer, and the $15h$ length in the wake region comes from the experimental observation (Gough and Hancock, 1996) that the spanwise Kármán vortices are weakened and decay away at about $10h$ downstream of the trailing edge. The computational domain extends some distance upstream of

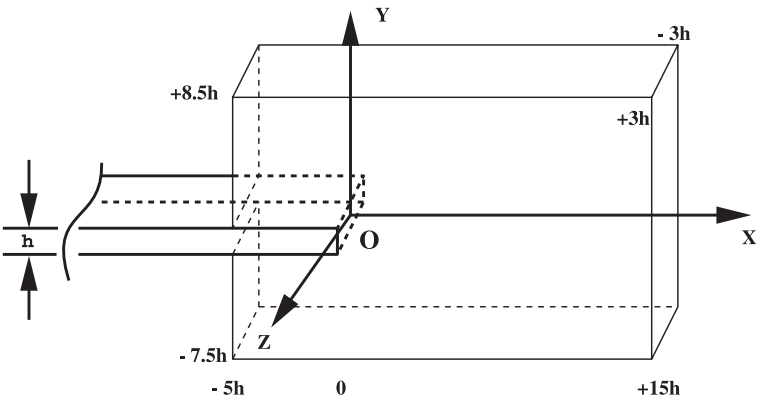

Figure 6. Computational box for the trailing edge flow simulation.

the trailing edge, thus permitting the boundary layer flow upstream of the separation points to be influenced by the large-scale unsteady motions in the wake. Hence it is possible to follow in a natural way the progression from a boundary layer flow to a wake flow. The box length in the wall-normal direction (denoted as L_Y) is set to be $16h$, with $8.5h$ in the upper side and $7.5h$ in the lower side individually. This asymmetric arrangement was chosen because of the simple decomposition of the computational domain and the corresponding high computational efficiency on the Cray-T3D and T3E parallel machines; the influence of this arrangement on the computed flow has been checked and found to be minor.

Compared with the inflow turbulent boundary layer thickness $\delta_{99} \simeq 6.42h$, the box length is sufficiently large to let the incoming boundary layers develop and grow along the $5h$ length plate before meeting at the trailing edge. The spanwise length (denoted as L_Z) is $6h$, the same as in the "precursor" turbulent boundary layer simulation. The effects of the computational box size are examined in Section 4.2, especially for the lower part of the box in the wall-normal direction where the domain is more restrictive.

To fit the simulation on a parallel computer such as the Cray-T3D/E the baseline computational box is decomposed uniformly into 4 parts in the streamwise direction, 16 parts in the wall-normal direction and 4 parts in the spanwise direction. This results in a total of 256 blocks (see Figure 7(a)). The trailing edge geometry occupies 4 blocks while 252 blocks are in the flow field. Such a domain decomposition is designed to get a higher computational efficiency when using the Cray-T3D/E computer, which normally supplies the processors in groups of 2^n.

For the baseline computation a grid of $32 \times 16 \times 16$, which leads to five grid levels in the multi-grid Poisson solver, is used in each block. The total number of grid points in the three directions is $128 \times 256 \times 64$. The grid spacing ratio in the three directions is $2.5 : 1 : 1.5$. Based on wall units the grid scales of the inlet turbulent boundary layer are $\Delta x^+ = 7.81$, $\Delta y^+ = 3.13$, $\Delta z^+ = 4.69$. It is not initially clear whether this grid resolution is sufficient. Detailed studies on the grid resolution issues are carried out in Section 4.3.

The boundary conditions are set up as follows. At the inflow plane the velocities are prescribed in the slice data taken from the "precursor" turbulent boundary layer simulation. A linear interpolation between the neighbouring inflow planes is used to find out the instantaneous inflow data when performing the trailing edge simulation, because different time steps have been used in the "precursor" and "successor" simulations. The outflow is treated by the widely used convective boundary condition, which allows the disturbances in the wake to leave the computational box smoothly. On the solid wall surface the no-slip condition is applied. The upper and lower boundaries use a free-slip condition.

A parallel multi-block code is used for the trailing edge flow simulation, in which, except for the pressure solution, the same numerical method as described in Section 2 is applied. The code is parallelized in a highly efficient manner and a flexible multi-block mapping strategy is developed to deal with the flow domain containing the complex-geometry. Based on these, a multi-grid algorithm is used for solving the pressure Poisson equation. For details of the parallelization and multi-grid Poisson solver, refer to Thomas and Williams (1997). The code has been applied to a variety of flow problems, giving results that are in agreement with the published computational and experimental data well (see Thomas and Williams, 1999a,b). For the rectangular trailing edge problem a test calculation has been carried out with a two-dimensional laminar

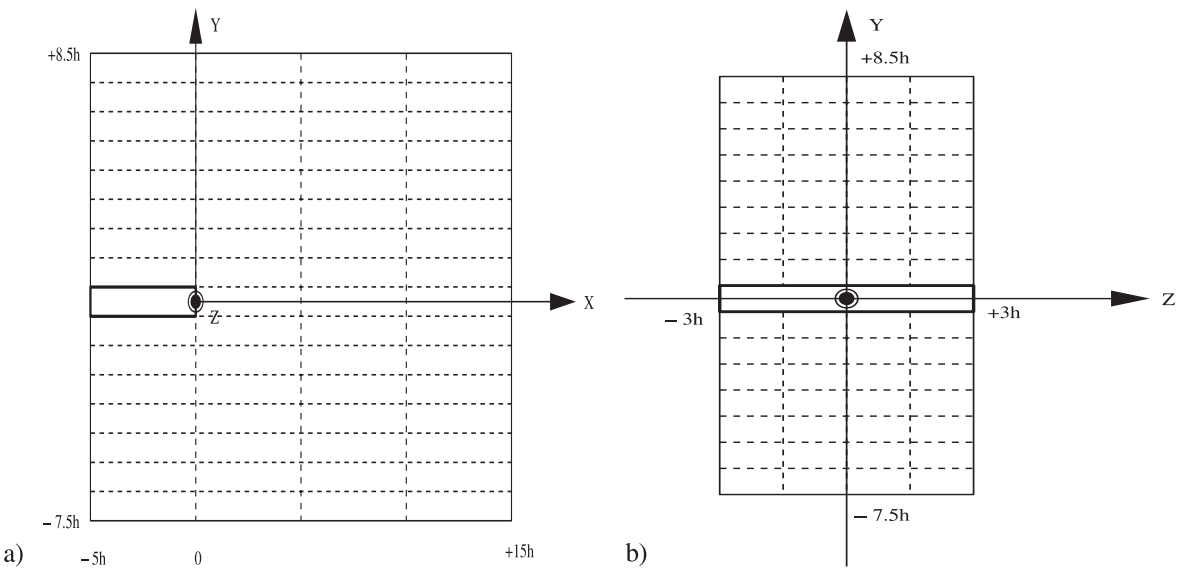

Figure 7. Domain decomposition and slice arrangements for the trailing edge flow simulation in the X–Y plane (a) and at the inflow plane (b).

incoming flow at a Reynolds number of 200 (based on the trailing edge thickness h) and results agree well with those of Hannemann and Oertel (1989) for the same flow.

4.2. Effects of Domain Size

In order to obtain a general understanding of the wake development after the trailing edge, we first look at the features revealed by statistical quantities. As an example, Figure 8(a) shows contours of the streamwise mean velocity U in the X–Y plane. The flow past the rectangular trailing edge geometry produces a recirculation zone. This can be observed more clearly by viewing the velocity vector field in the near trailing edge region as in Figure 8(b). The size of the recirculation region is defined by the distance between the trailing edge end plane and a stagnation point in the flow field labelled "S" (see Figure 8(b)) and it is about $2h$.

To study in detail the effects of the domain size on the computational results, a baseline case A has been carried out first, followed by two additional cases, namely case B, with a 50% longer box in the streamwise direction, and case C, with a 50% wider box in the wall-normal direction (see Table 1). Figure 9(a) gives the comparison of streamwise mean velocity U distributions along the centreline of the trailing edge. For three cases the maximum reverse flow (10% free-stream velocity U_e), the size of the recirculation region ($2h$) and the overall variations are very similar. The mean velocity U recovers quickly after the recirculation and then more slowly down to 50% freestream velocity at about $10h$ downstream. The differences at the outlet plane are most likely due to the effect of the numerical treatment there, but are generally very small.

Further comparisons are carried out along the wall-normal direction at seven streamwise stations in particular: two in the boundary layer region (i.e. $x/h = -3.047,\ -1.016$) and five in the wake region (i.e. $x/h = 1.016,\ 3.047,\ 5.078,\ 8.045,\ 12.109$), including one location in the recirculation region.

Figure 9(b) shows a comparison of the streamwise mean velocity U against the axis y/h, which is measured from the centreline of the trailing edge with the origin of successive profiles shifted forward by one unit. In the turbulent boundary layer only the upper part is plotted while the data in the wake region is drawn with the upper half of the whole profiles. (Results from the lower part have been compared and they are similar to those in the upper part. Hence the influence from the asymmetric arrangement in the wall-normal direction is minor.) At stations 1 and 2 the profiles show typical turbulent boundary layer characteristics. In the recirculation region at station 3 the streamwise velocity has negative values at the centreline where the reverse flow happens. From stations 4 to 7, the wake profiles evolve and the velocity at the centreline position increases up to about 55% U_e at the outlet plane. Figure 9(c) shows the square root of kinetic energy ($\sqrt{k}$) comparisons. Small differences are found only at station 3 in the recirculation region otherwise the agreements of the three

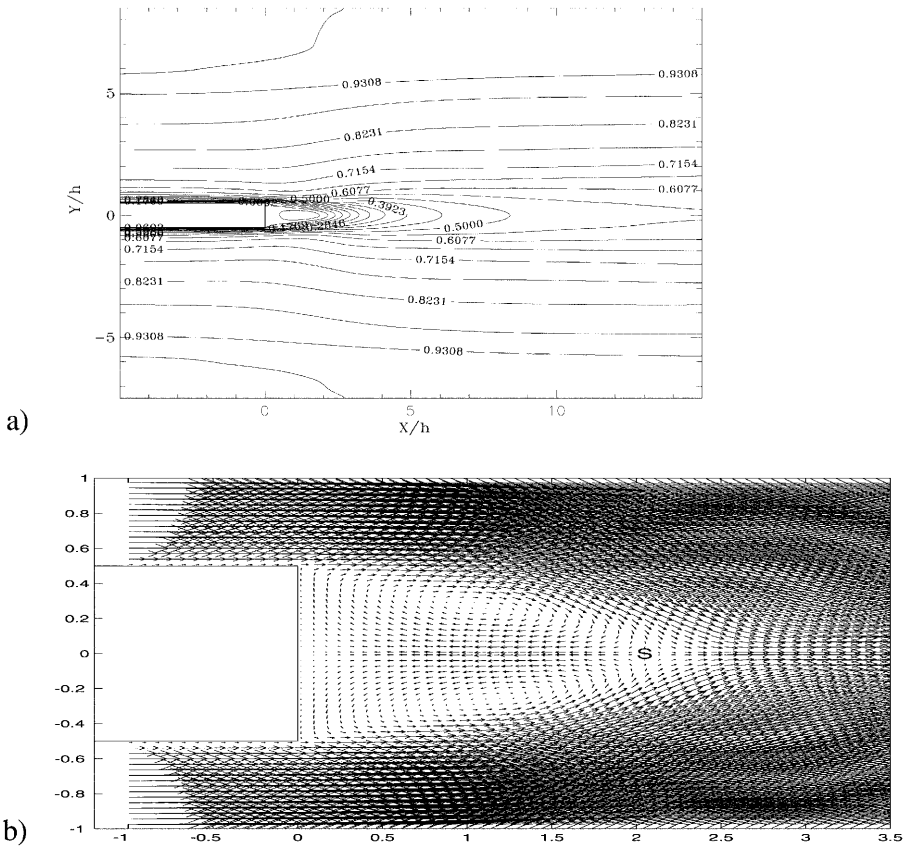

Figure 8. Mean velocity distributions in the X–Y plane (non-dimensionalized with U_e and h). (a) Contour plot; (b) Vector plot in near wall region with "S" representing a zero-velocity point in the flow field (data plotted every second point).

cases are good. As observed from the above the domain size change does not produce obvious effects on the main features of the wake development and the kinetic energy transport. The results appear more sensitive to L_Y than L_X, probably because this changes the potential flow slightly. Similar conclusions can be made from the results in Figure 9(d) of the Reynolds stress $-\langle uv \rangle$ comparisons, from which the maximum peak value of the Reynolds stress appears at station 4 and then gradually diminishes downstream. Along the centreline it is always zero as required by the symmetry condition.

It can be concluded that computations with a longer box length either in the streamwise or in the wall-normal directions do not have a significant effect on the mean and turbulence statistics. Hence the basic box length arrangement (i.e. $20h \times 16h \times 6h$ in all three directions) is concluded to be sufficiently large for the present trailing edge flow simulations and is used for the following grid resolution studies.

4.3. Grid Resolution Studies

Normally we require ten or more grid points within $y^+ \leq 10$ (i.e. the viscous sublayer) for DNS of near wall flow. This requirement comes from the experience with stretched grid methods. A better criteria may be the number of grid points in the buffer layer $10 < y^+ \leq 30$, where typical simulations have 10–15 points. In the baseline simulation (case A) there are 256 points equally distributed in the length of $16h$ which results in a Δy^+ of about 3.13 and only 3 points in the sublayer and 6 points in the buffer layer. This raises the question as to whether the flow in the near wall region has been properly resolved.

A mesh doubling strategy has been used to investigate the grid resolution issues both in the boundary layer and wake regions. Three cases have been run, namely case D, with double the number of grid points in the streamwise direction, case E, with double the number of grid points in the wall-normal direction, and case F, with double the number of grid points in the spanwise direction (see Table 1 for details).

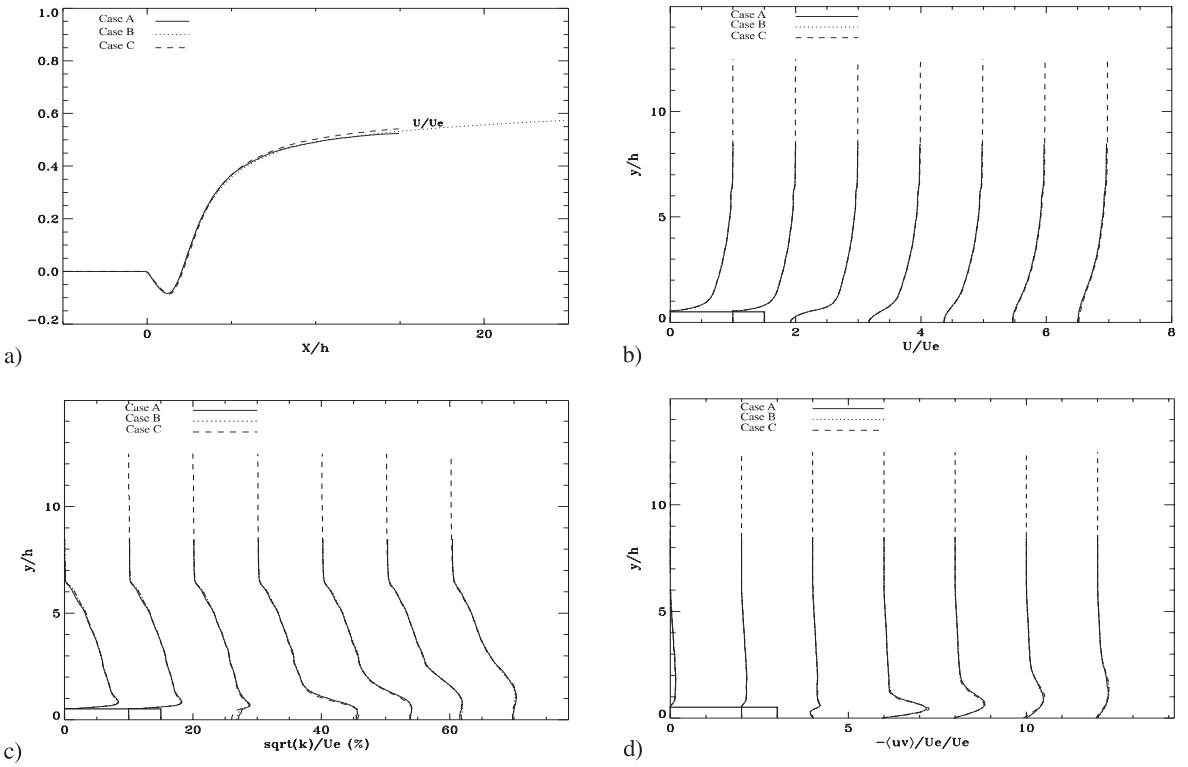

Figure 9. Results from domain size dependency study. (a) Streamwise mean velocity U distributions along the centreline where $y = 0$. (b) Mean velocity U profiles at seven streamwise stations, i.e. $x/h = -3.047$, -1.016, 1.016, 3.047, 5.078, 8.045, 12.109. (c) Square root value of turbulence kinetic energy. (d) Reynolds stress $-\langle uv \rangle$.

Table 1. Run cases for the trailing edge flow simulation investigating the effects of domain size and grid resolution. (Note: there are eight blocks in case H compared with four blocks in other cases in the streamwise direction.)

Case	Domain size $L_X \times L_Y \times L_Z$	Domain grids $N_x \times N_y \times N_z$	Block grids $n_x \times n_y \times n_z$
A	$20h \times 16h \times 6h$	$128 \times 256 \times 64$	$32 \times 16 \times 16$
B	$30h \times 16h \times 6h$	$192 \times 256 \times 64$	$32 \times 16 \times 16$
C	$20h \times 24h \times 6h$	$128 \times 384 \times 64$	$32 \times 16 \times 16$
D	$20h \times 16h \times 6h$	$256 \times 256 \times 64$	$64 \times 16 \times 16$
E	$20h \times 16h \times 6h$	$128 \times 512 \times 64$	$32 \times 32 \times 16$
F	$20h \times 16h \times 6h$	$128 \times 256 \times 128$	$32 \times 16 \times 32$
G	$20h \times 16h \times 6h$	$256 \times 512 \times 64$	$64 \times 32 \times 16$
H	$20h \times 16h \times 6h$	$512 \times 1024 \times 128$	$64 \times 64 \times 32$

Figure 10 gives a comparison of the mean velocity distribution along the centreline and mean velocity, square root of turbulence kinetic energy and Reynolds stress on various cross-sections (see Table 2 for the definition of the seven stations).

In the boundary layer region (at stations 1 and 2), the agreement among cases A, D and F is good. This gives the conclusion that the boundary layer flow of the baseline simulation (case A) has been properly resolved both in the streamwise and spanwise directions. By further grid refinement the results have not shown much improvement. To check the grid resolution we may compare the grid spacing at station 1 ($\Delta x^+ = 7.81$ and $\Delta z^+ = 4.69$) in the present simulation (case A) with that of Spalart and Leonard (1985) ($\Delta x^+ = 13$ and $\Delta z^+ = 6.5$). Our simulation with a finite difference method has about 70% and 40% more grid points in the x- and z-directions, respectively, compared with Spalart and Leonard who used a spectral method. However, finite difference methods typically require about twice the number of grid points to achieve similar results.

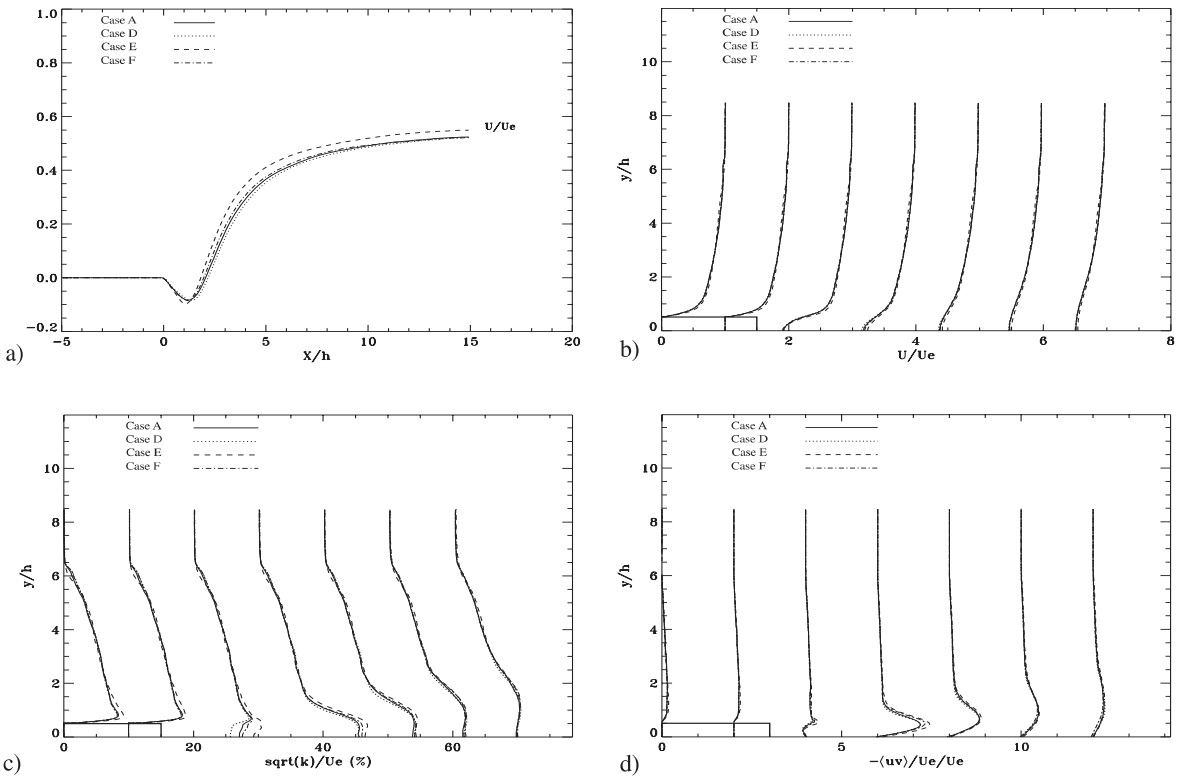

Figure 10. Results from grid resolution study. (a) Streamwise mean velocity U distributions along the centreline where $y = 0$. (b) Mean velocity U profiles at seven streamwise stations (for definition see Figure 9). (c) Square root value of turbulence kinetic energy. (d) Reynolds stress $-\langle uv \rangle$.

With such a factor of extra points, the results from the simulation are expected to be comparable based on our previous experience of channel flow finite difference simulation (Sandham, 1994). By contrast the flow in the wall-normal direction is not better resolved in case A. Doubling the points (case E) does improve the simulation results, but still may not be enough, and further refinement is desirable for this part of the flow in the boundary layer region in particular.

In the wake region (at stations 3–7) clear differences are evident in the simulations, due to either influence from the upstream flow in the boundary layer or poor resolution locally in the wake region. It can be seen from Figure 10(a),(b) that the streamwise mean velocity U of case E produces a narrower recirculation region and a higher maximum reverse flow. It also recovers more quickly than other cases and reaches a higher value at the outlet plane. Results from cases D and F are similar to those from the baseline simulation (case A). In the kinetic energy comparison of Figure 10(c) the maximum difference happens at station 3 where a lower value appears in case D and a higher value in case E. Results from case F agree well with that from case A. The difference appears to be reduced at station 4 and downstream, at stations 5–7, where the agreement is generally good. Similar conclusions can be made from Figure 10(d). It is useful to develop rules of thumb for the grid resolution requirement for the wake flow simulation to supplement those already known and applied in the turbulent boundary layer flow simulation. We therefore present the grid size in wake units denoted here in a form as $\Delta\tilde{x}_i = \Delta x_i \, \delta U_m / \nu$ with the help of the grid spacing Δx_i, mean velocity deficit δU_m and the kinematic viscosity of the fluid ν. The plane wake DNS of Moser *et al.* (1998) could be regarded as a good reference and the grid resolution from which has been estimated as $\Delta\tilde{x} \approx 98$ and $\Delta\tilde{y} \approx 82$. Results in the z-direction are not available but it can be assumed to be of the same order as in the y-direction. Comparing with the present simulation, for example case A, we have the grid spacing in wake units of $\Delta\tilde{x} = 167$, $\Delta\tilde{y} = 67$ and $\Delta\tilde{z} = 100$ at station 3 and $\Delta\tilde{x} = 126$, $\Delta\tilde{y} = 50$ and $\Delta\tilde{z} = 76$ at station 4. It can be seen clearly that in case A the flow in the near-wake region has not been properly resolved in the streamwise direction at stations 3 and 4, while in the wall-normal (y) direction the flow is well-resolved at all stations with resolution comparable with that estimated from Moser *et al.*'s simulation. This is due to the very strict requirement for

Table 2. Comparisons of grid resolutions in wall and wake units at selected streamwise stations.

		Cases					
		A	D	E	F	G	H
Station 1	u_τ (%)	4.986	4.799	5.132	4.823	5.097	5.085
($x = -3.047$)	Δx^+	7.790	3.749	8.019	7.536	3.982	1.986
	Δy^+	3.116	2.999	1.603	3.015	1.593	0.794
	Δz^+	4.674	4.499	4.811	2.261	4.779	2.384
Station 2	u_τ (%)	5.329	5.091	5.599	5.209	5.495	5.489
($x = -1.016$)	Δx^+	8.326	3.978	8.748	8.139	4.293	2.144
	Δy^+	3.330	3.182	1.749	3.255	1.717	0.857
	Δz^+	4.996	4.773	5.250	2.442	5.152	2.573
Station 3	δU_m	1.070	1.055	1.100	1.076	1.072	1.072
($x = 1.016$)	b	1.328	1.430	1.186	1.342	1.270	1.272
	$\Delta\tilde{x}$	167.179	82.450	171.960	168.146	83.809	41.887
	$\Delta\tilde{y}$	66.871	65.960	34.392	67.258	33.523	16.755
	$\Delta\tilde{z}$	100.307	98.940	103.176	50.444	100.570	50.264
Station 4	δU_m	0.808	0.935	0.692	0.789	0.770	0.795
($x = 3.047$)	b	1.882	1.542	2.252	2.040	1.852	1.762
	$\Delta\tilde{x}$	126.270	73.009	108.171	123.236	60.174	31.068
	$\Delta\tilde{y}$	50.508	58.407	21.634	49.294	24.069	12.427
	$\Delta\tilde{z}$	75.762	87.611	64.903	36.971	72.208	37.282
Station 5	δU_m	0.602	0.669	0.539	0.598	0.563	0.573
($x = 5.078$)	b	3.164	2.738	3.522	3.318	3.256	3.184
	$\Delta\tilde{x}$	94.011	52.267	84.204	93.497	43.993	22.394
	$\Delta\tilde{y}$	37.604	41.814	16.841	37.398	17.597	8.957
	$\Delta\tilde{z}$	56.407	62.720	50.523	28.049	52.791	26.873
Station 6	δU_m	0.503	0.529	0.460	0.499	0.470	0.471
($x = 8.045$)	b	4.014	3.988	4.402	4.144	4.190	4.174
	$\Delta\tilde{x}$	78.681	41.335	71.802	78.101	36.761	18.404
	$\Delta\tilde{y}$	31.473	33.068	14.360	31.240	14.704	7.362
	$\Delta\tilde{z}$	47.209	49.602	43.081	23.430	44.113	22.085
Station 7	δU_m	0.448	0.464	0.417	0.455	0.428	0.423
($x = 12.109$)	b	4.612	4.646	5.204	4.632	4.728	4.882
	$\Delta\tilde{x}$	69.990	36.238	65.128	71.208	33.441	16.521
	$\Delta\tilde{y}$	27.996	28.991	13.026	28.483	13.376	6.608
	$\Delta\tilde{z}$	41.994	43.486	39.077	21.362	40.130	19.826

the grid resolution in the boundary layer region, with the same grid points used in the wake. In the spanwise direction the flow is less well-resolved at station 3 but well-resolved at station 4.

Based on the discussion of the three grid resolution studies above it was felt necessary to carry out further simulations in which the flow in all three directions was better resolved both in the boundary layer, where further grid refinement in the wall-normal direction is still required, and the wake region, where further grid refinement in the streamwise direction is needed. Two high-resolution simulations were carried out, namely case G, with $256 \times 512 \times 64$ ($\sim 8.4 \times 10^6$) grid points, and case H, with $512 \times 1024 \times 128$ ($\sim 6.7 \times 10^7$) grid points, in which the simulation has double the number of points in all directions compared with case G (see Table 1).

Figure 11(a) gives a comparison of the streamwise mean velocity along the centreline. Figure 11(b)–(f) shows the comparisons of various quantities U, $U_{\rm rms}$, $V_{\rm rms}$, $W_{\rm rms}$ and $-\langle uv \rangle$ on seven cross-sections defined as before.

In the boundary layer region (i.e. stations 1 and 2), the agreement between cases G and H is very good. This gives the conclusion that the boundary layer flow in the case G simulation has been properly resolved in all the streamwise, wall-normal and spanwise directions. The grid refinement even in the wall-normal direction does not have much effect on the results. By looking at the grid resolution comparisons at stations 1 and 2 in Table 2 it is clear that in the case G simulation there are only 6 grid points in the sublayer but 13

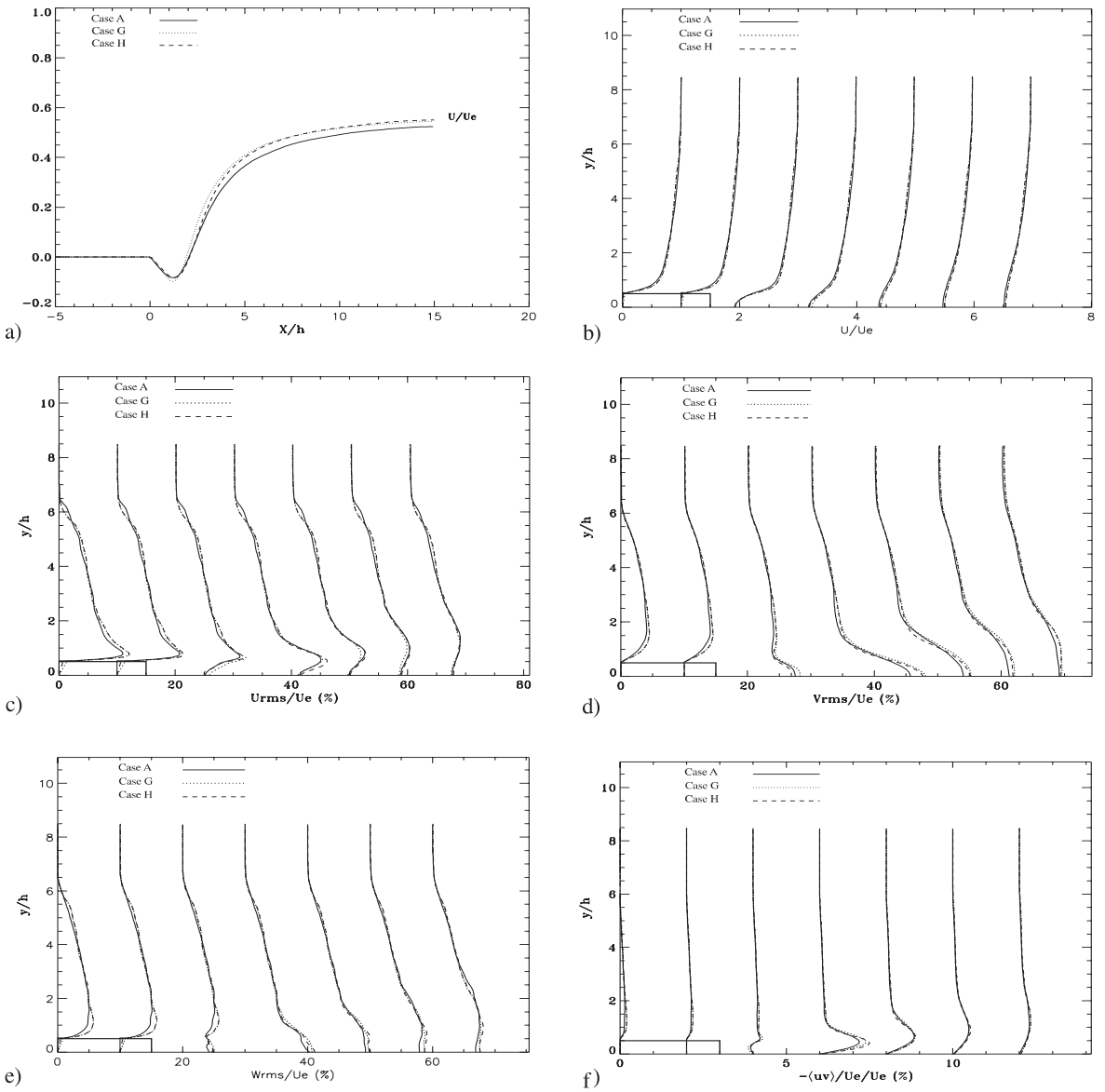

Figure 11. Results from high-resolution simulations. (a) Streamwise mean velocity U distributions along the centreline where $y = 0$. (b) Mean velocity profiles at seven streamwise stations (for definition see Figure 9). (c) Turbulence intensity $U_{\rm rms}$ in the streamwise direction. (d) Turbulence intensity $V_{\rm rms}$ in the wall-normal direction. (e) Turbulence intensity $W_{\rm rms}$ in the spanwise direction. (f) Reynolds stress $-\langle uv\rangle$.

points in the buffer layer. However, the results are comparable with those from simulation case H, which has 12 grid points in the sublayer and 24 points in the buffer layer. This conclusion gives further support to our previous argument that the number of grid points in the buffer layer is more important than the number in the sublayer.

In the near-wake region agreement between cases G and H is generally good (see Figure 11(a),(b)) with small deviations near the recirculation region. In Figure 11(c) there are differences at stations 3, 4 and 5 where case H has a slightly lower value at centreline at station 3 and a higher peak at stations 4 and 5. The differences are reduced at stations 6 and 7. Similar phenomena can be observed from Figure 11(d) as well. It seems that the influence of grid refinement in the streamwise direction is slightly stronger than that in the wall-normal direction in the near-wake region. Results from Figure 11(e),(f) agree well at all stations. Figure 12 gives a surface pressure comparison of cases A, G and H, from which the convergence on successive grids is demonstrated. Although there is a lack of existing published experiments for a cross-plotting com-

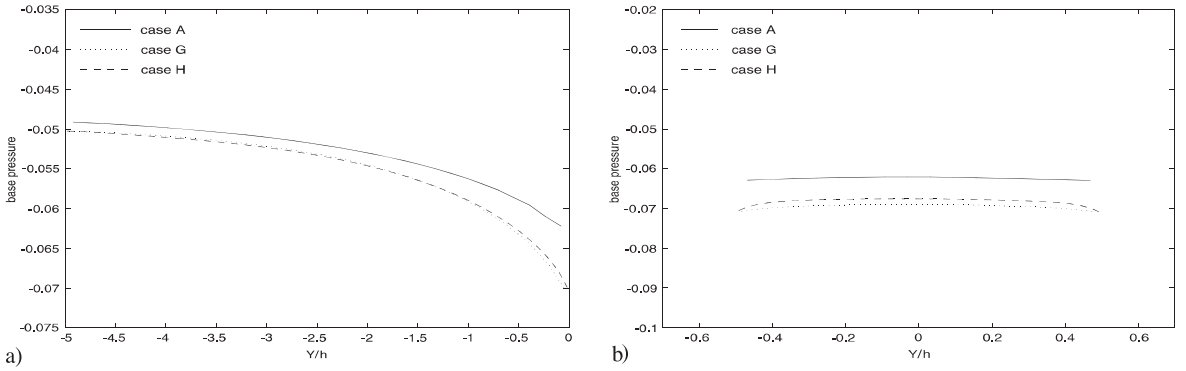

Figure 12. Mean pressure distributions over the trailing edge geometry along the plate (a) and at the base (b).

parison, results from the experimental study of Gough and Hancock (1996) (with more experimental data available in Gao *et al.* (1996)), with different incoming flow conditions but the same configuration, have been used for a qualitative comparison. Results from the present simulation show the correct order of magnitude along the centreline and also the correct trends and profiles at streamwise stations for all the variables analysed.

Results from this grid resolution study are summarized in Table 2, with data presented in terms of the wake units defined above and compared at stations 3–7. Also given are the mean velocity deficit δU_m and the wake half-width $b(x)$. Alternatively, the grid resolution can be expressed in terms of the Kolmogorov microscale $\eta \equiv (\nu^3/\varepsilon)^{1/4}$, where ε is the turbulence energy dissipation rate. As a reference we estimate $\Delta\bar{x} = \Delta x/\eta \approx 15$ for a plane wake DNS (Moser *et al.*, 1998). In the present simulations case G gives the $\Delta\bar{x}$ value of 13.79, 9.79, 6.72, 5.50, 4.99 at stations 3–7, and case H gives the value of 6.88, 5.07, 3.42, 2.76, 2.44, respectively. It is clear that in general the present simulation (case H) is better resolved in both the near- and far-wake regions.

4.4. Visualization of Instantaneous Flow Structures

Figure 13(a)–(c) shows the instantaneous velocity (u, v and w) contours in an X–Y plane at $z = 0$. The flow behind the trailing edge shows clear evidence of asymmetric vortex shedding. In particular steep gradients in w-contours are found in the central part of the near wake (Figure 13(c)) which are believed to be related to the distorted flow structures locally.

The three-dimensional flow structure is visualized by snapshots of the instantaneous flow in a region close to the trailing edge. This section of the computational box has a size of $X_L = 10h$ ($x = -2h \sim 8h$), $Y_L = 6h$ ($y = -3h \sim 3h$) and $Z_L = 6h$ ($z = -3h \sim 3h$). In order to identify the large-scale spanwise Kármán vortices and the small-scale streamwise vortices clearly, we define two vortex identifications: an iso-surface on which the pressure has a constant value enclosing a low pressure core indicating the large-scale vortex structures, and an iso-surface of the second invariant of the velocity gradient tensor representing the small-scale streamwise vortices, and given by

$$\Pi = \frac{\partial u_i}{\partial x_j}\frac{\partial u_j}{\partial x_i}\,, \tag{16}$$

which marks regions of fluid where the flow is locally dominated by rotation. Both identifications illustrate vortex structures with the pressure indicator emphasizing the large-scale vortices and the second invariant (Π) indicator giving the small-scale vortices. In the visualization the dark shading shows the spanwise vortices and the light shading represents the streamwise vortices. Figure 14(a) shows a top view of the flow. It can be seen that coherent large-scale spanwise vortices are formed just after the trailing edge and the well-known Kármán vortex street exists in the wake region. The appearance of vortex shedding after the trailing edge is mainly due to the reverse flow and is related to the existence of absolute instability by linear stability theory (Hannemann and Oertel, 1989). This, in turn, causes the global oscillation of

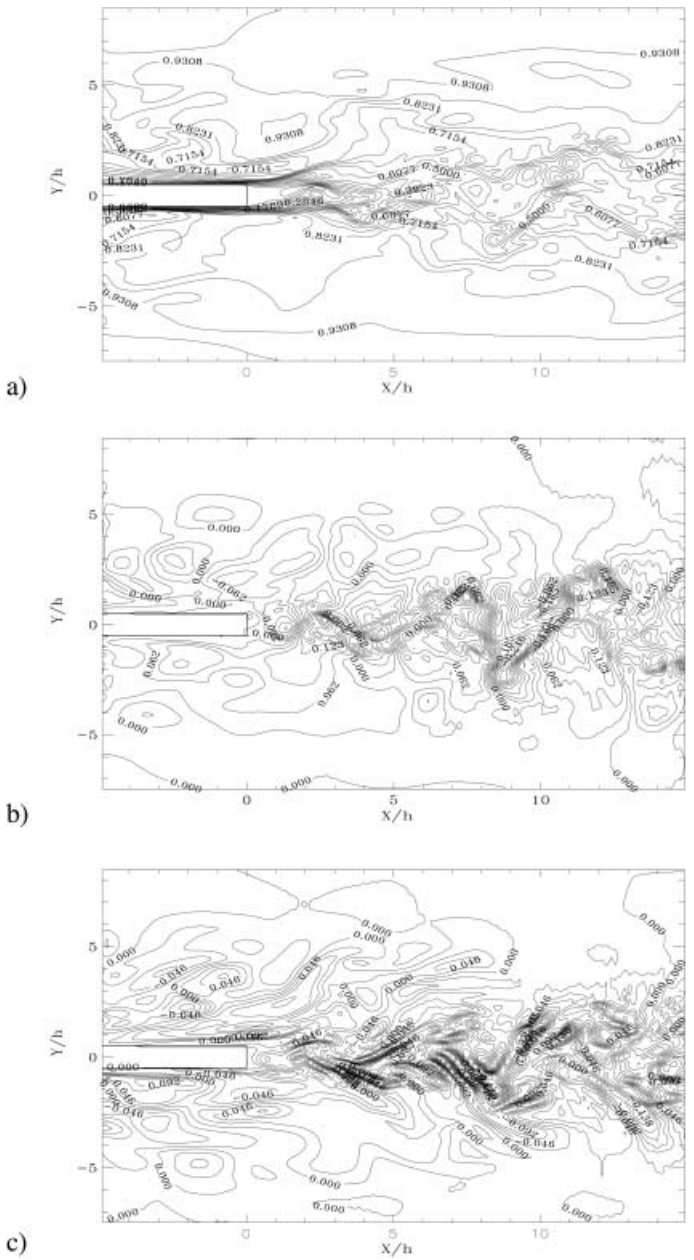

Figure 13. Contours of instantaneous velocity in the $X-Y$ plane at $z = 0.0$. (a) Streamwise u-velocity, (b) wall-normal v-velocity and (c) spanwise w-velocity.

the flow and the formation of Kármán vortex streets. It should be noted that although the vortices in the wake all originated from the upstream turbulent boundary layer, they undergo further re-distribution and become stronger in the near wake. As a result stronger streamwise vortices are visualized in the wake than in the boundary layer region using the same indicator. The existence of Kármán vortices and their influence on the streamwise small-scale vortices is the main reason. From the visualization it can be seen that the streamwise vortices are stretched between two neighbouring spanwise Kármán vortices along the direction of principal strain field. Further, the vortex shedding in the present simulation is not purely periodic and not perfectly coherent in the spanwise direction over the whole wake region. This is due to the three-dimensionality of the incoming turbulent flow and the evolution of the three-dimensional wake. The bending of the Kármán vortices in the wake also illustrates a three-dimensional structure. Ultimately the spanwise vortices are scrambled and eventually destroyed by the intense small-scale streamwise vortices in the

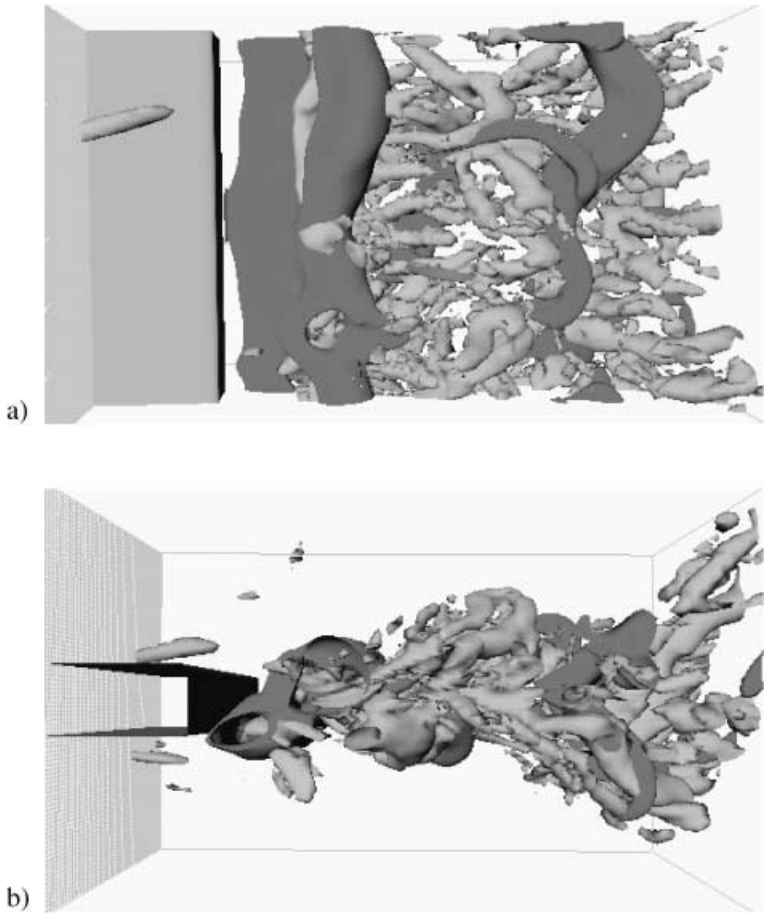

Figure 14. Instantaneous flow structures from case G simulation. Dark shading: low pressure; light shading: second invariant. (a) A top view and (b) a side view.

far-wake region. These vortex interactions between large-scale spanwise Kármán vortices and small-scale streamwise vortices have also been observed by Najarr and Balachandar (1998) in a numerical investigation of flow over a normal flat plate at Reynolds number 250. The present observations are qualitatively similar.

To assess the vortex shedding in the flow over the trailing edge with a finite thickness, a complementary simulation was carried out with the same configuration and grids as case G but setting the trailing edge thickness h to zero (i.e. an infinitely thin plate); with this geometry the flow is believed to possess only a weak absolute instability in the near-wake region due to a lack of reverse flow region. Figure 15 gives a side view of the instantaneous flow field with the same vortex indicators and shading defined as before. The streamwise vortices in the turbulent boundary layer and wake regions are clearly shown. Due to the zero plate thickness and consequent weak absolute instability, no clear spanwise vortex structures are observed after the trailing edge. The strength of vortices in the wake region is not greatly increased when moving from the boundary layer into the wake, whereas it does increase for a finite thickness trailing edge.

4.5. Spectral Analysis

To investigate the vortex shedding behind the trailing edge, we determine the shedding frequency using a force coefficient defined by

$$C_{\mathrm{F}} \simeq \frac{1}{\frac{1}{2}\rho U_e^2 A_o} \int_0^{L_Z} \int_{-5h}^{0} (p_{\mathrm{l}} - p_{\mathrm{u}})\, \mathrm{d}x\, \mathrm{d}z, \tag{17}$$

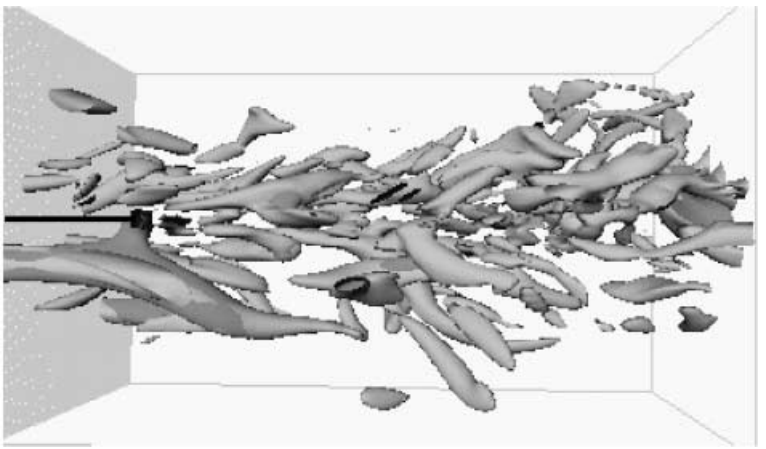

Figure 15. Instantaneous flow structures from the simulation over an infinitely thin plate (a side-view). Shading defined as in Figure 14.

where the integral is performed over the plate horizontal surface area of $A_o = 5hL_Z$ and $(p_\mathrm{l} - p_\mathrm{u})$ indicates the difference of pressure between the lower and upper plates. We accept a slight error by truncating the semi-infinite domain to $5h$ but this does not affect the interpretation of the results and is not considered serious.

Figure 16(a) gives the time history of the force coefficient C_F over a time interval of about $180h/U_e$, from which the unsteady and irregular shedding is quite clearly evident. The shedding period can be estimated by measuring the average time between two neighbouring peaks; this is approximately $10h/U_e$, hence the shedding frequency f_s is about $0.1U_e/h$. The Strouhal number $S_t \equiv f_\mathrm{s}h/U_e$, based on the trailing edge thickness and freestream velocity, is thus estimated as ~ 0.1. A more precise estimate of shedding frequency can be obtained from a spectral analysis of C_F. The power spectrum of C_F (see Figure 16(b)) shows the main shedding frequency at the more precise estimate of 0.118, which is in good agreement with the value of ~ 0.12 estimated from the experiment by Gough and Hancock (1996), but significantly smaller than typically found in cylinder flows (typically in the range $S_t \sim 0.15$–0.2). It is interesting to note that Najarr and Balachandar (1998) found a Strouhal number of 0.143 when experimentally investigating the flow past a thin plate placed normal to the flow at a Reynolds number (based on plate dimensions) of about 250. The shedding behaviour exhibited in the simulation is quasi-periodic; it has a superficial appearance of periodicity, but never repeats itself, and also exhibits short bursts of strong shedding with intervals of relatively weak shedding in between. These characteristics are typical of observations made of turbulent experimental bluff body flows, see for example Najarr and Balachandar (1998), and are qualitatively distinct from the almost perfectly periodic behaviour found in strictly two-dimensional calculations of turbulent flows (for example, by various unsteady RANS methods). This suggests that three-dimensionality is an essential feature of turbulent bluff body flows even when the flow structure appears capable of being represented in an essentially two-dimensional way. These findings have implications for computational procedures that aim to predict unsteady loading patterns on structures subjected to turbulent flow conditions.

4.6. Turbulence Kinetic Energy Budgets

Following the standard procedure as that described in Yao *et al.* (1999), an energy budget analysis can be made based on the turbulence kinetic energy equation as

$$\frac{\partial k}{\partial t} + R = P - \epsilon - \left(J^u_{i,i} + J^p_{i,i} + J^v_{i,i}\right), \tag{18}$$

where $R = \overline{u_i}(\partial k/\partial x_i)$ is the convection term, $P = -\overline{u'_i u'_j}(\partial \overline{u_i}/\partial x_j)$ is the production,

$$\epsilon = \frac{1}{Re}\overline{\frac{\partial u'_i}{\partial x_j}\left(\frac{\partial u'_i}{\partial x_j} + \frac{\partial u'_j}{\partial x_i}\right)} \tag{19}$$

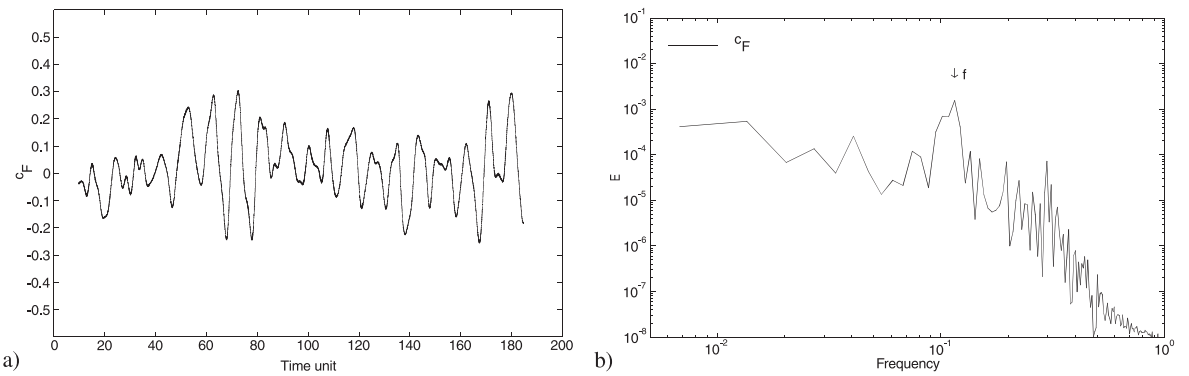

Figure 16. The time sequence of pressure coefficient in the wall-normal direction of the trailing edge geometry. (a) A time history of about 180 time units. (b) A spectral analysis.

is the dissipation and

$$J^u_{i,i} = \frac{\partial(\overline{u'_i u'_j u'_j}/2)}{\partial x_i}, \qquad J^p_{i,i} = \frac{\partial(\overline{p' u'_i})}{\partial x_i}, \qquad J^v_{i,i} = -\frac{1}{Re}\frac{\partial}{\partial x_i}\left(\frac{\partial k}{\partial x_i} + \frac{\partial \overline{u'_i u'_j}}{\partial x_j}\right) \tag{20}$$

are turbulence triple-moment, pressure and viscous transport terms, respectively. The turbulence kinetic energy budget analysis has been carried out for case G, results from which can be found in Yao *et al.* (1999) and case H, results from which are given here in Figure 17, corresponding to stations 2–5.

In the boundary layer region alongside the plate at station 2 (see Figure 17(a)) the dominant term in the energy balance is the production term; this takes its maximum value at about $y^+ \sim 10$. Closer to the plate, $y^+ < 10$, the viscous transport term dominates. The dissipation term remains the energy drain over the whole thickness of the boundary layer, and outside the buffer layer, $y^+ > 30$, the balance is (mostly) between the production and dissipation terms, so that $P \approx \epsilon$. The overall energy balance indicated by the residual error in the summation appears to be quite small.

In the middle of the recirculation region (Figure 17(b)) the production has a negative peak in the reverse flow area and a positive peak away from the central region. Comparing Figure 17(b) with Figure 17(a) it can be seen that the convection term and the pressure transport term grow rapidly and reach high values, approximately the same as the production term. In contrast, the viscous transport term approaches zero due to the absence of the solid wall. The energy balance is dominated by the convective transport, pressure transport and production terms. After the recirculation region (Figure 17(c)), the production continues to increase and exceeds the magnitudes of other terms, and becomes the largest term in the budget. The triple-moment transport term has increased in contrast to that of Figure 17(b), with a negative peak near the centreline and a positive peak away from it. A useful observation is that the pressure transport term in the central part of the wake changes sign when moving from a position inside the recirculation ($x = h$) to a position after that ($x = 3h$). This is discussed further in Yao *et al.* (2000). Further downstream (Figure 17(d)) all terms are decreasing, and the production, convection and triple-moment terms are still dominant. Overall, good budget balances are achieved.

5. Conclusions

A direct numerical simulation (DNS) has been used for the study of a turbulent flow over a rectangular trailing edge geometry at a Reynolds number 1000, based on the freestream quantities and the trailing edge thickness h. A turbulent boundary layer flow simulation was conducted to supply the inflow boundary conditions for the trailing edge flow simulation. A parallel complex-geometry finite difference DNS code was used for the latter. The effects of domain size and grid resolution were studied. It is concluded from the simulations that the domain size change does not have a significant effect on the results and consequently the basic computational box (with a size of $20h \times 16h \times 6h$ in the three directions) is sufficiently large for the present

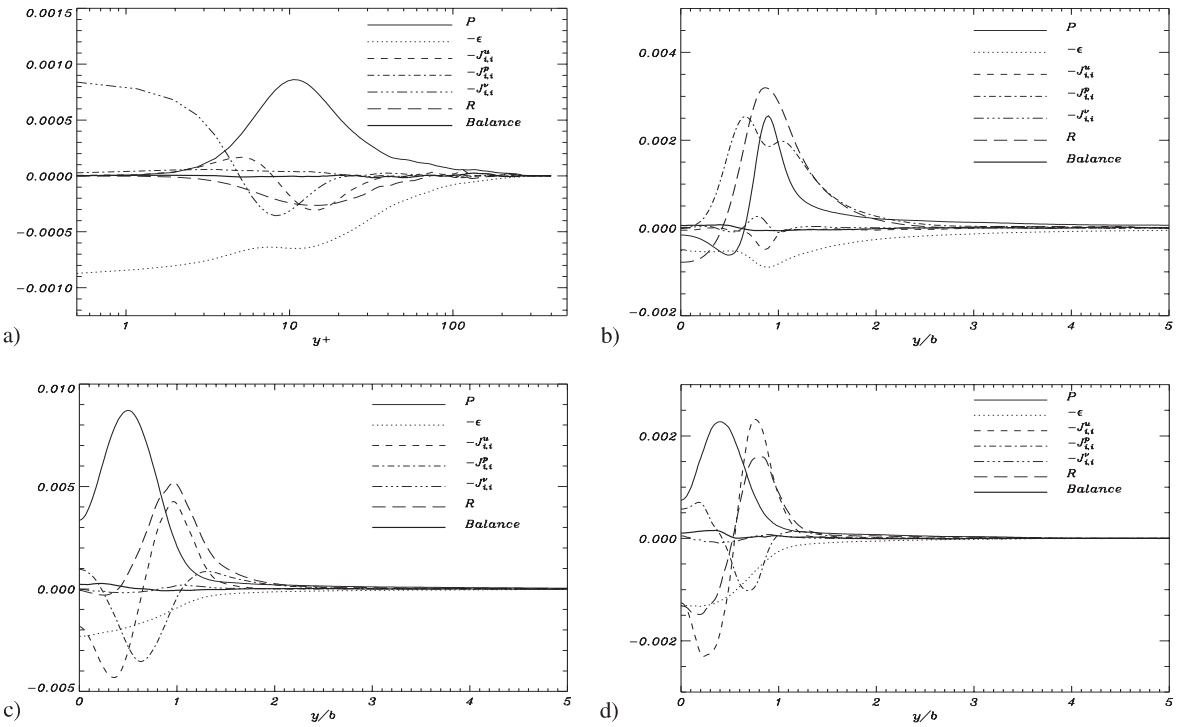

Figure 17. Turbulence kinetic energy budgets from case H. (a) At $x = -h$ (in the boundary layer), (b) at $x = h$ (in the recirculation region), (c) at $x = 3h$ (after the recirculation region) and (d) at $x = 5h$ (in the wake region).

simulation. Using more points in the wall-normal direction the results are improved, especially in the near wall and wake regions. Different flows present different requirements for grid resolution: in the boundary layer flow the grid resolution in the wall-normal direction is crucial, while in the wake flow additional grid resolutions in the streamwise and spanwise directions are further required. The far-wake region presents no additional problems. A rule of thumb for the near-wake simulation is that the grid spacing in wake units $\Delta\tilde{x}_i$ (where $\Delta\tilde{x}_i = \Delta x_i\, \delta U_m/\nu$) should be less than 100, based on the present DNS and other simulations of plane wake flow. Examination of the mean flow reveals that a recirculation zone exists after the trailing edge with a length of about $2h$. The turbulence quantities ($\sqrt{k}$, $U_{\rm rms}$, $V_{\rm rms}$, $W_{\rm rms}$) and Reynolds stress ($-\langle uv\rangle$) results have been compared at seven streamwise stations, in both the boundary layer and wake regions. Two high-resolution simulations with grid points of $256 \times 512 \times 64$ ($\sim 8.4 \times 10^6$) and $512 \times 1024 \times 128$ ($\sim 6.7 \times 10^7$), respectively, have been carried out to investigate the flow physics. The complex instantaneous flow structure has been presented by both two-dimensional contours and three-dimensional flow field snapshots. The interactions between the large-scale spanwise Kármán vortices and the small-scale streamwise vortices has been visualized. The pressure distributions over the trailing edge are compared for the high-resolution cases and a spectral analysis using the force coefficient in the wall-normal direction is also shown, illustrating the main shedding frequency, characterized with a Strouhal number equal to 0.118, which is close to that found in experiments with a similar flow condition. Finally a turbulence kinetic energy budget analysis has been carried out. A good budget balance has been achieved, giving further validation for this DNS study, and key features such as negative production and strong pressure transport effects have been identified.

References

Bearman, P.W. (1998). Developments in the understanding of bluff body flows. *JSME Int. J., Ser. B*, **41**(1), 103–114.

Black, W.K. (1975). A Statistical Description of Pressure and Velocity Fields at the Trailing Edge of a Flat Strut. DTNSRDC Report 4241, David Taylor Naval Ship R&D Center, Bethesda, MD.

Gao, S.A., Voke, P.R., and Gough, T.D. (1996). Turbulent simulation of a flat plate boundary layer and near wake. In *Proc. Second ERCOFTAC Workshop on Direct and Large Eddy Simulation*, pp. 115–124.

Gough, T.D., and Hancock, P.E. (1996). Lower Reynolds number turbulent near wakes. In *Advances in Turbulence VI* (S. Gavrilakis *et al.*, eds.), pp. 445–448. Kluwer, Dordrecht.

Hannemann, K., Lynn, T.B., and Strykowski, P.J. (1986). Experimental investigation of the wake behind a flat plate with and without the influence of base bleed. *DFVLR IB*, **A26**, 221–86.

Hannemann, K., and Oertel, H. (1989). Numerical simulation of the absolutely and convectively unstable wake. *J. Fluid Mech.*, **199**, 55–88.

Klebanoff, P.S. (1954). Characteristics of Turbulence in a Boundary Layer with Zero Pressure Gradient. *NACA Technical Note TN-3178*.

Kleiser, L., and Schumann, U. (1980). Treatment of incompressibility and boundary layer conditions in 3D numerical spectral simulations of plane channel flows. In *Proc. 3rd GAMM Conf. on Numerical Methods in Fluid Mechanics* (E.H. Hirschel, ed.) pp. 165–173. Vieweg Verlag, Braunschweig.

Lund, T.S., Wu, X., and Squires, K.D. (1996). On the generation of turbulent inflow conditions for boundary layer simulations. In *Annual Research Briefs – 1996*, pp. 281–295. Center for Turbulence Research, Stanford University/NASA Ames.

Lund, T.S., Wu, X., and Squires, K.D. (1998). Generation of turbulent inflow data for spatially-developing boundary layer simulations. *J. Comput. Phys.*, **140**(2), 233–258.

Moser, R.D., Rogers, M.M., and Ewing, D.W. (1998). Self-similarity of time-evolving plane wakes. *J. Fluid Mech.*, **367**, 255–289.

Najarr, F.M., and Balachandar, S. (1998). Low-frequency unsteadiness in the wake of a normal flat plate. *J. Fluid Mech.*, **370**, 101–147.

Nakayama, A. (1984). Measurements of attached and separated turbulent flows in the trailing-edge region of airfoils. In *Numerical and Physical Aspects of Aerodynamic Flows II* (T. Cebeci, ed.). Springer-Verlag, Berlin.

Purtell, L.P., Klebanoff, P.S., and Buckley, F.T. (1981). Turbulent boundary layer at low Reynolds number. *Phys. Fluids*, **24**(5), 802–811.

Roshko, A. (1993). Perspectives on bluff body aerodynamics. *J. Wind Eng. Indust. Eng.*, **49**, 79–100.

Sandham, N.D. (1994). Resolution Requirement for Direct Numerical Simulation of Near Wall Turbulent Flow Using Finite Difference. Report *QMW-EP-1097*, Dept. of Engineering, Queen Mary and Westfield College, University of London.

Spalart, P.R. (1988). Direct simulation of a turbulent boundary layer up to $Re_\theta = 1410$. *J. Fluid Mech.*, **187**, 61–98.

Spalart, P.R., and Leonard, A. (1985). Direct numerical simulation of equilibrium turbulent boundary layers. In *Proc. 5th Symp. on Turbulent Shear Flows*, pp. 234–252. Ithaca, NY, Aug. 7–9.

Thomas, T.G., and Williams, J.J.R. (1997). Development of a parallel code to simulate skewed flow over a bluff body. *J. Wind Eng. Indust. Eng.*, **67**&**68**, 155–167.

Thomas, T.G., and Williams, J.J.R. (1999a). Simulation of skewed turbulent flow past a surface mounted cube. *J. Wind Eng. Indust. Aerodyn.*, **81**, 347–360.

Thomas, T.G., and Williams, J.J.R. (1999b). Large eddy simulation of vortex shedding from cubic obstacle. *J. Aerospace Eng., ASCE*, **12**(4), 113–121.

Thompson, B.E., and Whitelaw, J.H. (1985). Characteristics of a trailing-edge flow with turbulent boundary-layer separation. *J. Fluid Mech.*, **157**, 305–326.

Viswanath, P.R., and Brown, J.L. (1983). Separating trailing-edge flow at a transonic Mach number. *AIAA J.*, **21**, 801–807.

Wang, M. (1997). Progress in large-edge simulation of trailing-edge turbulence and aeroacoustics. In *Annual Research Briefs – 1997*, pp. 37–49. Center for Turbulence Research, Stanford University/NASA Ames.

Wu, X.H., and Squires, K.D. (1998). Numerical investigation of the turbulent boundary layer over a bump. *J. Fluid Mech.*, **362**, 229–271.

Yao, Y.F., Sandham, N.D., Thomas, T.G., and Williams, J.J.R. (1999). Study of turbulent trailing-edge flow using direct numerical simulation. In *Proc. Int. Symp. of Turbulence Shear Flow Phenomenon – 1*, pp. 627–632.

Yao, Y.F., Savill, A.M., Sandham, N.D., and Dawes, W.N. (2000). Simulation of a turbulent trailing-edge flow using unsteady RANS and DNS. In *Proc. 3rd Int. Symp. on Turbulence, Heat and Mass Transfer*, pp. 463–470. Nagoya, Japan.